Supporting Information

Bilsborough et al. 10.1073/pnas.1015162108

SI Materials and Methods

Genetics. Double mutants analyzed included *axr1-3;cuc2-3*, *bdl/BDL;cuc2-3*, *pin1-1;mir164a-4*, *pin1-1;axr1-3*, and *as1-1;cuc2-3*. All double mutants were generated in the same manner as the following example. For *axr1-3;cuc2-3*, *axr1-3* plants from the F_2 generation of a cross between *axr1-3* and *cuc2-3* homozygotes were self-pollinated to generate F_3 families that segregated *axr1-3;cuc2-3* double mutants. *axr1-3;as1-1;cuc2-3* triple mutants were generated in the following way: *axr1-3;as1-1* plants from the F_2 generation of a cross between *axr1-3;as1-1* and *axr1-3;cuc2-3* homozygotes were self-pollinated to generate F_3 families that segregated *axr1-3;as1-1;cuc2-3* triple mutants.

Transgenes analyzed in single mutants included: *axr1-3;MIR164A::GUS*, *bdl/BDL;MIR164A::GUS*, *axr1-3;35S::MIR164A*, *bdl/BDL:35S::MIR164A*, *pin1-1;CUC2::GUS*, *pin1-1;CUC2::CUC2:VENUS*, *mir164a-4;BP::GUS*, *cuc2-3;BP::GUS*, *as1-1;35S::MIR164A*, and *pin1-7;CUC2gm-4*. All lines were generated in the same manner as the following example. For *axr1-3;MIR164A::GUS*, GUS-positive *axr1-3* plants from the F_2 generation of a cross between *axr1-3* and *MIR164A::GUS* homozygotes were self-pollinated to generate F_3 families. Transgenes analyzed in double mutants included *axr1-3;cuc2-3;BP::GUS*, *as1-1;cuc2-3;BP::GUS*, and *axr1-3;as1-1;35S::MIR164A*. All lines were generated in the same manner as the following example. For *axr1-3;cuc2-3;BP::GUS*, GUS-positive *axr1-3;cuc2-3* homozygotes from the F_2 generation of a cross between *cuc2-3* and *axr1-3;BP::GUS* homozygotes were self-pollinated to generate F_3 families. *axr1-3;as1-1;cuc2-3;BP::GUS* triple mutants were generated in the following way: GUS-positive *axr1-3;as1-1* homozygotes from the F_2 generation of a cross between *axr1-3;as1-1;BP::GUS* and *cuc2-3* homozygotes were self-pollinated to generate F_3 families that segregated *axr1-3;as1-1;cuc2-3;BP::GUS*. The double reporter line *DR5::GFP;CUC2::CUC2:VENUS* was generated in the following way: *DR5::GFP*-positive plants from the F_2 generation of a cross between *DR5::GFP* and *CUC2::CUC2:VENUS* homozygotes were self-pollinated to generate F_3 families that segregated *DR5::GFP;CUC2::CUC2:VENUS* plants.

Plant Growth Conditions. Plants were grown on a medium of soil: vermiculite in a 1:1 ratio in a greenhouse with supplemented lighting (days, 18 h, 20 °C; nights, 6 h, 16 °C).

Plasmid Construction and Analysis of Transgenics. To generate the *AtML1*-pMDC32 vector, the *ATML* promoter was amplified from an *ATML1::GFP* plasmid (1) using ATML1-HindIII-F and ATML1-KpnI-R primers and subcloned into PCRblunt (Invitrogen). The 35S promoter was removed from pMDC32 (2) by a HindIII/KpnI double digestion and replaced with the subcloned *AtML1* promoter.

For the *AtML1::PIN1:GFP* construct, a *PIN1:GFP* cassette was PCR amplified from a *PIN1::PIN1:GFP* plasmid (3) using PIN1-F and PIN1-R primers and subcloned into pCR8/GW-TOPO (Invitrogen). The *PIN1:GFP* cassette was then recombined into *AtML1*-pMDC32. The *AtML1::PIN1:GFP* construct was transformed into plants segregating *pin1-7*. Thirteen independent transgenic lines of *AtML1::PIN1:GFP* were obtained, of which 3 were confirmed to be mutant for *pin1-7*.

For the *AtML1::CUC2:VENUS* construct, a *CUC2:VENUS* cassette was PCR amplified from a *CUC2::CUC2:VENUS* plasmid (3) using CUC2-F and VENUS-R primers and subcloned into pCR8/GW-TOPO (Invitrogen). The *CUC2:VENUS* cassette was then recombined into *AtML1*-pMDC32. The construct was transformed into Col plants and three broad classes of transformants were observed: cup-shaped cotyledons and shootless, fused cotyledons and shootless, and leaf-producing plants (not shootless). For the former category, quantitative RT-PCR showed that the phenotype does not result from cosuppression. For the latter category, 41 independent transgenic lines were recovered, of which 9 had smooth leaf margins and 6 had asymmetric leaf lamina. *MIR164A::GFP* was used to control for effects of hygromycin on development.

The *CUC2::CUC2:VENUS* (3) construct was transformed into wild-type Col plants. A homozygous T3 line was crossed to *cuc2-3* mutants, and resulting F_3 *cuc2-3;CUC2::CUC2:VENUS* plants were genotyped using CUC2-F and VENUS-R primers to confirm the presence of the *CUC2::CUC2:VENUS* transgene. *cuc2-3;CUC2::CUC2:VENUS* plants had rescued serration development, indicating that the *CUC2::CUC2:VENUS* construct is functional.

Primers used include the following:

ATML1-HindIII-F AAGCTTATCAAAGAAAAAACAAGAA
ATML1-KpnI-RCTGGTACCGGATTCAGGGAGTTTCTTTAA
PIN1-F GGGATCCCCAAAAGAGGAAACACGAATG
PIN1-R GCGGTACCTCCCTCTTCACCACTTCTCTC
CUC2-F ATGGACATTCCGTATTACCAC
VENUS-R ATGGACATTCCGTATTACCAC
PIN1-2F CCAACACTCTAGTCATGGGGATA
PIN1-4F CTGAGAGTATGGAGATAGAC.

Chemical Treatments. Indole-3-acetic acid (IAA; Sigma) was dissolved in ethanol to a stock concentration of 10 mM and added to Murishuge–Skoog (MS) liquid medium to a final concentration of 1 μM. A total of 0.002% ethanol in MS liquid medium was used for controls. *CUC2::GUS* plants grown on sterile MS plates were incubated in either MS liquid medium + 1 μM IAA or control liquid medium for 24 h before being GUS stained.

2,4-dichlorophenoxyacetic acid (2,4-D; Sigma) was dissolved in dimethyl sulfoxide (DMSO) to a stock concentration of 1 mM and diluted to 10 μM in ddH_2O + 0.02% Silwet. ddH_2O + 1% DMSO + 0.02% Silwet was used for controls. Plants grown on soil were sprayed with either 10 μM 2,4-D or control spray once per day for a week.

Microscopy. Scanning electron microscopy (SEM) and confocal microscopy were carried out as previously described (4). SEM samples were analyzed using a JSM-5510 microscope (Jeol). Seedlings for confocal microscopy were mounted and observed in water without fixation. Single-plane sections or projections from stacks of 5–20 sections are presented in Figs. 1 *A–C* and *F* and *G*, 2 *A–H*, 3 *H* and *I*, 4*G*, and Figs. S1 *A–F* and S2 *A–E*. To image GFP we used the 458-nm argon laser of a Zeiss LSM510 Meta microscope with a 646- to 700-nm filter for the chlorophyll channel and a band-pass 475- to 525-nm filter for GFP. To image VENUS we used the 514-nm argon laser with a 647- to 754-nm filter for the chlorophyll channel and a band-pass 535- to 590-nm filter (single localization). To image GFP in a double localization with VENUS, we used the 488-nm argon laser of a Leica DM6000 CS microscope with a band-pass 495- to 509-nm filter for GFP and a 632- to 731-nm filter for the chlorophyll channel. To image VENUS in a double localization with GFP, we used the 514-nm argon laser of a Leica DM6000 CS microscope with a band-pass 520- to 592-nm filter.

Quantitative RT-PCR Analysis. Total RNA (1 μg) extracted from 10-d-old seedling tissue was DNaseI treated and used for cDNA synthesis with an oligo(dT) primer and SuperScript reverse transcriptase (Invitrogen). cDNA was amplified on the ABI PRISM 7300 Sequence Detection System (Applied Biosystems). Amplification reactions were prepared with the SYBR-Green PCR Master Kit (Applied Biosystems), according to the manufacturer's specifications, with 0.4 μM primer and 10 μL 1:10-diluted cDNA per reaction. Each reaction was made in triplicate, and each experiment was repeated three times. The efficiency of each set of primers and calculation of the level of induction was determined according to Pfaffl (5). Error bars represent the SE calculated on biological replicates. Expression levels were normalized with values obtained for the *ORNITHINE TRANSCARBAMILASE* (*OTC*) gene, which was used as an internal reference gene as described by Cnops (6).

Primers used include the following:

OTCqRT-F TGAAGGGACAAAGGTTGTGTATGTT
OTCqRT-R CGCAGACAAAGTGGAATGGA
CUC2qRT-F CAGCCGTAGCACCAACACAA
CUC2qRT-R GTCTAAGCCCAAGGCCCCGTAGTA
MIR164AqRT-F CCCTCATGTGCTTGGAAATG
MIR164AqRT-R GCAAATGAGACGGATTTCGTG.

GUS Staining. GUS staining was performed as previously described (7), using 1 mM 5-bromo-4-chloro-3-indoly-β-D-glucuronic acid (Invitrogen) supplied with ferrocyanide and ferricyanide salts (2 mM *ATHB-8::GUS* and 10 mM *CUC2::GUS* and *MIR164A::GUS*). Reactions were terminated with 95% ethanol, and leaves were dissected, mounted in 50% glycerol, and viewed using either differential interference microscopy (DIC) or dark-field microscopy.

Leaf Clearings, Silhouettes, and Quantification of Leaf Dissection Index. Leaf clearings were performed by incubating leaves in excess 7:1 ethanol:acetic acid solution overnight at room temperature. Leaves were then transferred to chloral hydrate solution and were mounted on slides with chloral hydrate solution before viewing with dark-field microscopy. For leaf silhouettes, leaves were adhered to white paper using clear adhesive and were then digitally scanned. Leaf area and perimeter were calculated from silhouettes using ImageJ software. Leaf dissection index was then determined by using the formula ((perimeter squared)/(4π × area)) (8).

Detailed Model Description. ***Molecular processes.*** Many morphogenetic processes that regulate leaf form take place on the leaf margin (see experimental results in the main text). Consequently, we model a leaf as a single file of cells on the leaf margin. For simplicity, all cells in the model are assumed to have unit volume, and all interfaces between adjacent cells (cell walls and membranes) have unit area. Under these assumptions, the balance law capturing the changes of auxin concentration c_i in cell i has the form (9)

$$\frac{dc_i}{dt} = \sigma(H - c_i) - \mu c_i - \sum_j \Phi_{i\to j} + \Phi_{\text{ext}}. \qquad \text{[S1]}$$

The term $\sigma(H - c_i)$ models local auxin production, which is assumed to asymptotically approach target level H with the rates controlled by coefficient σ. The term μc_i captures auxin turnover at the rate controlled by coefficient μ. Nonzero values of the term Φ_{ext} make it possible to simulate exogenous application of auxin (Fig. 5*J*). Finally, the sum $\sum_j \Phi_{i\to j}$ represents auxin transport along the leaf margin as the sum of fluxes $\Phi_{i\to j}$ through the faces separating cell i from its neighbors j. The fluxes are captured by the equation (10–12)

$$\Phi_{i\to j} = Tc_i\left[\text{PIN}_{i\to j}\right] - Tc_j\left[\text{PIN}_{j\to i}\right] + D\left(c_i - c_j\right), \qquad \text{[S2]}$$

where $[\text{PIN}_{i\to j}]$ is the concentration of PIN proteins in the membrane of cell i abutting cell j, T characterizes the efficiency of PIN-dependent polar transport, and D is a coefficient of diffusion. (Within this paper symbols PIN and CUC denote PIN1 and CUC2 proteins, as no other members of PIN and CUC protein families are considered.) A flux $\Phi_{i\to j}$ is assumed to be positive if it represents net efflux from cell i to cell j and negative otherwise. Potentially, PIN proteins within each cell are allocated to cell membranes according to the up-the-gradient polarization model (12, 13), using the formula proposed by Smith et al. (13):

$$\left[\text{PIN}_{i\to j}\right]_{\text{potential}} = [\text{PIN}_i]\frac{b^{c_i}}{\sum_k b^{c_k}}. \qquad \text{[S3]}$$

The total amount of PIN proteins in a cell i, denoted $[\text{PIN}_i]$, is thus distributed between cell membrane segments according to an exponential function of auxin concentrations in the neighboring cells. The sum in the denominator, ranging over all cells k adjacent to cell i, normalizes the results, such that concentrations of PIN proteins allocated to individual segments of the membrane add up to the total concentration $[\text{PIN}_i]$. Following the experimental results reported in the main text (Fig. 2 *G* and *H*), we further assume that PIN (re)polarization in cell i takes place only if the concentration of CUC proteins in this cell exceeds a threshold value Th_{CUC}. In the opposite case, the allocation of PIN to membrane segments in cell i remains constant:

$$\left[\text{PIN}_{i\to j}\right] = \begin{cases} \left[\text{PIN}_{i\to j}\right]_{\text{potential}} & \text{if} \quad [\text{CUC}_i] > \text{Th}_{\text{CUC}} \\ \text{const} & \text{otherwise.} \end{cases} \qquad \text{[S4]}$$

Changes in CUC concentration are modeled by the equation

$$\frac{d[\text{CUC}_i]}{dt} = \frac{\rho_{\text{CUC}}}{1 + \kappa_{\text{CUC}} c_i}\cdot [\text{CUC}_i] - \left(\nu + \nu_{\text{IAA}} c_i\right)[\text{CUC}_i]. \qquad \text{[S5]}$$

This equation specifies changes in CUC concentrations as an aggregate result of CUC production (first term) and turnover (second term). We assume that CUC production is controlled by parameter ρ_{CUC} and is down-regulated by auxin. This down-regulation represents an miRNA-independent effect of auxin on CUC, likely resulting from the regulation of CUC transcription by auxin. The sensitivity to auxin is controlled by parameter κ_{CUC}. The rate of auxin degradation is controlled by the auxin-independent term V and the auxin-dependent term $\nu_{\text{IAA}} c_i$. This latter term is meant to represent the effect of auxin-dependent degradation of CUC by *miR164*. To capture cell saturation with CUC, we further assume that CUC concentration cannot exceed a maximum value CUC_{MAX}.

Growth regulation. Leaf development is simulated using the boundary propagation methods (14), i.e., by propagating leaf margin in space over time. This process is carried out iteratively, by updating positions $(x_{i,j}, y_{i,j})$ of cell wall midpoints between adjacent cells i and j (except for the walls at the leaf base). On this basis, cell geometry is updated. A cell divides when its length (defined as the distance between the midpoints of the walls separating this cell from its neighbors along the margin) exceeds a threshold value $\text{Th}_{\text{length}}$. At this point, the cell is replaced by two daughter cells, which inherit the molecular state of the parent.

Margin propagation is simulated by adding margin displacement, which is locally controlled by simulated molecular processes, to an assumed background growth of the whole leaf. The displacement velocity $\vec{v}_{i,j} = (v^x_{i,j}, v^y_{i,j})$ of point $(x_{i,j}, y_{i,j})$ is calculated as

$$\vec{v}_{i,j} = f_{\text{IAA}}\left(\frac{c_i + c_j}{2}\right) f_{\text{CUC}}\left(\frac{[\text{CUC}_i] + [\text{CUC}_j]}{2}\right) h\left(y_{ij}\right)\vec{N}_{i,j}, \qquad \text{[S6]}$$

where $\vec{N}_{i,j}$ is the propagation directions normal to the margin and pointing outward (Fig. 5*B*). Function f_{IAA} captures the dependence of the propagation rate on the average concentration

of auxin in cells i and j. This velocity increases sigmoidally with the average auxin concentration in the adjacent cells i and j: Given $\Delta a = a_{\max} - a_{\min}$ and $\Delta c = c_{\max} - c_{\min}$, the function f_{IAA}

$$f_{\mathrm{IAA}}(c) = \begin{cases} a_{\min} & \text{if } c \le c_{\min} \\ -2\frac{\Delta a}{\Delta c^3}(c - c_{\min})^3 + \frac{\Delta a}{\Delta c^2}3(c - c_{\min})^2 + a_{\min} & \text{if } c_{\min} < c \le c_{\max} \\ a_{\max} & \text{if } c_{\max} < c. \end{cases} \quad \text{[S7]}$$

smoothly interpolates between the minimum value $a_{\min}$ and the maximum value $a_{\max}$ over the interval $[c_{\min}, c_{\max}]$ (Fig. S4 *A* and *B*) (15).

Function f_{CUC} captures the impact of the average CUC concentration in cells i and j on the propagation rate: Given $\Delta b = b_{\max} - b_{\min}$ and $\Delta[\mathrm{CUC}] = [\mathrm{CUC}]_{\max} - [\mathrm{CUC}]_{\min}$, this

$$f_{\mathrm{cuc}}([\mathrm{CUC}]) = \begin{cases} b_{\max} & \text{if } [\mathrm{CUC}] \le [\mathrm{CUC}]_{\min} \\ \Delta b\left(1 - \frac{[\mathrm{CUC}] - [\mathrm{CUC}]_{\min}}{\Delta[\mathrm{CUC}]}\right) + b_{\min} & \text{if } [\mathrm{CUC}]_{\min} < [\mathrm{CUC}] \le [\mathrm{CUC}]_{\max} \\ b_{\min} & \text{if } [\mathrm{CUC}]_{\max} < [\mathrm{CUC}]. \end{cases} \quad \text{[S8]}$$

function decreases linearly from the maximum value $b_{\max}$ for CUC concentrations less then the threshold $[\mathrm{CUC}]_{\min}$ to the minimum value $b_{\min}$ for CUC concentrations exceeding the threshold $[\mathrm{CUC}]_{\max}$ (Fig. S4*C*). We found that the piecewise linear function (Eq. **S8**) made it easier to explore the impact of CUC overexpression than a sigmoidal function of the form (Eq. **S7**), which could have also been used.

The margin propagation velocity $\vec{v}_{i,j}$ also depends on the distance $y_{i,j}$ of the point $(x_{i,j}, y_{i,j})$ from the base of the leaf. This dependency is captured by the function

$$h(y) = \begin{cases} h_{\max}\left(1 - \frac{y}{y_h}\right) & \text{if } 0 \le y < y_h \\ 0 & \text{if } y \ge y_h, \end{cases} \quad \text{[S9]}$$

where $h_{\max}, y_h > 0$ are parameters (Fig. S4*D*). This function reflects the reported spatiotemporal growth pattern of young *Arabidopsis* leaves, according to which cell division rates are highest $(h_{\max})$ near the leaf base $(y = 0)$, decrease as the distance from the base increases $(0 < y < y_h)$, and eventually drop to zero at the distal parts of the leaf $(y \ge y_h)$ (16, 17).

Margin displacement is superimposed on the background growth of the leaf blade, which is specified in terms of relative elementary rates of growth (RERG) (18, 19) in the x (lateral) and y (longitudinal) directions. We assume that these rates depend on the distance y from the leaf base in a manner similar to the function h (Eq. **S9**):

$$\mathrm{RERG}_X(x,y) = \begin{cases} a_X\left(1 - \frac{y}{\mathrm{Th}_X}\right) & \text{if } \mathrm{Th}_{\mathrm{PETIOLE}} \le y < \mathrm{Th}_X \\ 0 & \text{otherwise} \end{cases} \quad \text{[S10]}$$

$$\mathrm{RERG}_Y(x,y) = \begin{cases} a_Y\left(1 - \frac{y}{\mathrm{Th}_Y}\right) & \text{if } 0 \le y < \mathrm{Th}_Y \\ 0 & \text{otherwise.} \end{cases} \quad \text{[S11]}$$

Plots of these functions are shown in Fig. S4 *E*–*G*. The lateral growth of the leaf blade near the petiole is inhibited by molecular factors outside the scope of our model (20). This inhibition is needed to maintain a narrow base at its junction with the petiole (the petiole itself is not included in the model). The inhibition is simulated by assuming that the function RERG_X (Eq. **S10**) is zero near the leaf base $(y < \mathrm{Th}_{\mathrm{PETIOLE}})$.

The rate of displacement of a wall (i, j) between cells i and j in the transversal direction results from the integration of RERG_X along the x axis and the addition of the displacement due to marginal growth,

$$\frac{dx}{dt} = \int_0^x \mathrm{RERG}_X(s,y)ds + v_{ij}^x, . \quad \text{[S12]}$$

where y is the ordinate of the center of the wall between cells i and j. A similar formula applies to the displacement in the longitudinal direction:

$$\frac{dy}{dt} = \int_0^y \mathrm{RERG}_Y(x,s)ds + v_{ij}^y. \quad \text{[S13]}$$

Given the simple form of the RERG functions defined by Eqs. **S10** and **S11**, the integrals in Eqs. **S12** and **S13** have closed forms:

$$\int_0^x \mathrm{RERG}_X(s,y)ds = \begin{cases} a_X\left(1 - \frac{y}{\mathrm{Th}_X}\right)x & \text{if } \mathrm{Th}_{\mathrm{PETIOLE}} \le y < \mathrm{Th}_X \\ 0 & \text{otherwise} \end{cases} \quad \text{[S14]}$$

$$\int_0^y \mathrm{RERG}_Y(x,s)ds = \begin{cases} a_Y\left(y - \frac{y^2}{2\mathrm{Th}_Y}\right) & \text{if } 0 \le y < \mathrm{Th}_Y \\ a_Y\frac{\mathrm{Th}_Y}{2} & \text{otherwise.} \end{cases} \quad \text{[S15]}$$

As an example, the integral given by Eq. **S15** is shown in Fig. S4 *F* and *G*.

Implementation. All simulations (Fig. 5, Fig. S5, and Movies S1, S2, S3, S4, S5, S6, S7, S8, S9, S10, and S11) were specified in the L+C modeling language (21, 22), which is based on the mathematical formalism of L-systems (23, 24). At each stage of structure development, the differential equations composing the model (Eqs. **S1**, **S5**, **S12**, and **S13**) were solved numerically using forward Euler's integration. We used 50 integration steps for the molecular-level simulations (Eqs. **S1** and **S5**) per growth simulation step (Eqs. **S12** and **S13**). The adequacy of this scheme was verified by reducing the time steps fivefold; the same results were obtained. The simulations have been implemented and visualized using the software package L-studio (http://algorithmicbotany.org/lstudio).

Parameter values. Although estimates for the values of some parameters used in our simulations exist (e.g., refs. 12 and 25–27), most values are not yet known. Consequently, we use dimensionless parameters in our simulation, which is consistent with the qualitative nature of the presented model. The model produces serrated leaf forms for a wide range of parameter values: With some coordination between different parameters, most parameters can be significantly changed—even by several orders of magnitude—while qualitatively preserving the simulation results (not shown). The range of parameters is narrower (with some parameters, especially growth attributes, defined with the accuracy of $\pm 10\%$) if a specific leaf shape and number of serrations is to be generated, as was the case in the examples shown in the main text. Overall, the values in Tables S2 and S3 are reported to ensure reproducibility of our results, rather than estimate the physical values.

As noted in the main text, simulations start with the margin of a leaf primordium modeled as a sequential arrangement of eight cells, with CUC2 expressed in all cells, and auxin present in all cells except for the first and the last cell in the sequence. We have chosen initial conditions with uniform CUC2 distribution so that we can obtain a consistent state of the model (with CUC2 eliminated from the distal zone and PIN1 proteins pointing to the auxin maximum) automatically, instead of setting all attributes individually in each cell. The earliest developmental stage observed in our data (Fig. 1*A*) corresponds approximately to frame 20 of the simulations.

1. Gifford M-L, Dean S, Ingram G-C (2003) The Arabidopsis ACR4 gene plays a role in cell layer organisation during ovule integument and sepal margin development. *Development* 130:4249–4258.
2. Curtis M-D, Grossniklaus U (2003) A gateway cloning vector set for high-throughput functional analysis of genes in planta. *Plant Physiol* 133:462–469.
3. Heisler M-G, et al. (2005) Patterns of auxin transport and gene expression during primordium development revealed by live imaging of the Arabidopsis inflorescence meristem. *Curr Biol* 15:1899–1911.
4. Bowman J-L, Smyth D-R, Meyerowitz E-M (1991) Genetic interactions among floral homeotic genes of Arabidopsis. *Development* 112:1–20.
5. Pfaffl M-W (2001) A new mathematical model for relative quantification in real-time RT-PCR. *Nucleic Acids Res* 29:e45.
6. Cnops G, et al. (2004) The rotunda2 mutants identify a role for the LEUNIG gene in vegetative leaf morphogenesis. *J Exp Bot* 55:1529–1539.
7. Sessions A, Weigel D, Yanofsky M-F (1999) The Arabidopsis thaliana MERISTEM LAYER 1 promoter specifies epidermal expression in meristems and young primordia. *Plant J* 20:259–263.
8. Bai Y, Falk S, Schnittger A, Jakoby M-J, Hülskamp M (2010) Tissue layer specific regulation of leaf length and width in Arabidopsis as revealed by the cell autonomous action of ANGUSTIFOLIA. *Plant J* 61:191–199.
9. Prusinkiewicz P, et al. (2009) Control of bud activation by an auxin transport switch. *Proc Natl Acad Sci USA* 106:17431–17436.
10. Mitchison G-J (1981) The polar transport of auxin and vein patterns in plants. *Philos Trans R Soc B* 295:461–471.
11. Feugier F-G, Mochizuki A, Iwasa Y (2005) Self-organization of the vascular system in plant leaves: Inter-dependent dynamics of auxin flux and carrier proteins. *J Theor Biol* 236:366–375.
12. Jönsson H, Heisler M-G, Shapiro B-E, Meyerowitz E-M, Mjolsness E (2006) An auxin-driven polarized transport model for phyllotaxis. *Proc Natl Acad Sci USA* 103: 1633–1638.
13. Smith R-S, et al. (2006) A plausible model of phyllotaxis. *Proc Natl Acad Sci USA* 103: 1301–1306.
14. Sethian J (1999) *Level Set Methods and Fast Marching Methods: Evolving Interfaces in Computational Geometry, Fluid Mechanics, Computer Vision, and Materials Science* (Cambridge Univ Press, Cambridge, UK).
15. Prusinkiewicz P, Hammel M, Mjolsness E (1993) Animation of plant development. *Proceedings of SIGGRAPH* 93 (ACM SIGGRAPH, New York) pp 351–360.
16. Donnelly P-M, Bonetta D, Tsukaya H, Dengler R-E, Dengler N-G (1999) Cell cycling and cell enlargement in developing leaves of Arabidopsis. *Dev Biol* 215:407–419.
17. Rolland-Lagan A-G, Amin M, Pakulska M (2009) Quantifying leaf venation patterns: Two-dimensional maps. *Plant J* 57:195–205.
18. Richards O-W, Kavanagh A-J (1943) The analysis of the relative growth gradients and changing form of growing organisms: Illustrated by the tobacco leaf. *Am Nat* 77: 385–399.
19. Hejnowicz Z, Romberger J (1984) Growth tensor of plant organs. *J Theor Biol* 110: 93–114.
20. Tsukaya H (2006) Mechanism of leaf-shape determination. *Annu Rev Plant Biol* 57: 477–496.
21. Karwowski R, Prusinkiewicz P (2003) Design and implementation of the L+C modeling language. *Electron Notes Theor Comput Sci* 86:134–152.
22. Prusinkiewicz P, Karwowski R, Lane B (2007) *The L+C Plant Modelling Language* (Springer, Dordrecht, The Netherlands).
23. Lindenmayer A (1968) Mathematical models for cellular interaction in development, part I and II. *J Theor Biol* 18:280–315.
24. Prusinkiewicz P, Lindenmayer A (1990) *The Algorithmic Beauty of Plants* (Springer, New York).
25. Grieneisen V-A, Xu J, Marée A-F, Hogeweg P, Scheres B (2007) Auxin transport is sufficient to generate a maximum and gradient guiding root growth. *Nature* 449: 1008–1013.
26. Kramer E-M (2008) Computer models of auxin transport: A review and commentary. *J Exp Bot* 59:45–53.
27. Bayer E-M, et al. (2009) Integration of transport-based models for phyllotaxis and midvein formation. *Genes Dev* 23:373–384.

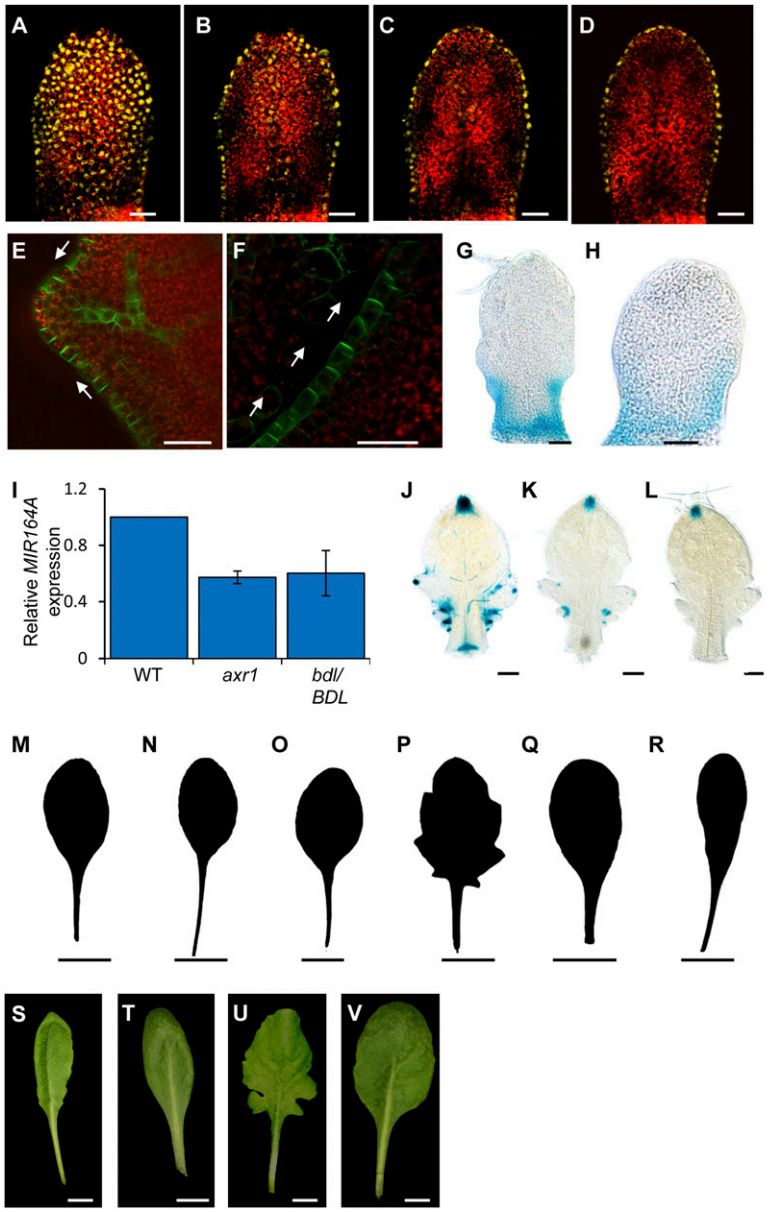

Fig. S1. Detailed expression analysis of *AtML1::CUC2:VENUS* and *PIN1::PIN1:GFP* and the regulation of *CUC2* and *MIR164A* expression by auxin. (*A*–*D*) Serial confocal optical sections of *AtML1::CUC2:VENUS* expression in a wild-type fifth rosette leaf 360 μm in length, proceeding from the epidermis inward at intervals of 9.2 μm. These sections confirm the L1 localization of the CUC2:VENUS fusion protein. (*E* and *F*) Confocal micrographs of *PIN1::PIN1:GFP* expression at the margin of fifth rosette leaves 250 μm in length in wild type (*E*) and *cuc2-3* (*F*). Arrows indicate direction of auxin flow. (*G* and *H*) *CUC2::GUS* staining in fifth rosette leaf of wild type 400 μm in length (*G*) and *pin1-7* 300 μm in length (*H*). (*I*) Quantitative RT-PCR analysis showed that *axr1-3* and *bdl/BDL* plants displayed reduced *MIR164A* gene expression compared with wild type. (*J*–*L*) *MIR164A::GUS* staining in sixth rosette leaf 400 μm in length of wild type (*J*), *axr1-3* (*K*), and *bdl/BDL* (*L*). (*M*–*O*) Overexpression of *MIR164A* under an auxin-independent promoter (*M*) was sufficient to prevent serration formation in *axr1-3;35S::MIR164A* (*N*) and *bdl/BDL;35S::MIR164A* plants (*O*). Thus, reduced *MIR164A* expression, and consequently elevated levels of *CUC2,* causes the deeply serrated leaf margins in *axr1-3* and *bdl/BDL* mutants. (*P*–*R*) *mir164a-4* (*P*), *pin1-1* (*Q*), and *pin1-1;mir164a-4* (*R*). (*S*–*V*) Sixth rosette leaf of wild type (*S*), *pin1-7* (*T*), *CUC2gm-4* (*U*), and *pin1-7;CUC2gm-4* (*V*). (Scale bars: *A*–*F*, 25 μm; *G*, *H*, and *J*–*L*, 50 μm; and *M*–*V*, 1 cm.) Error bars represent SE of mean from three biological replicates.

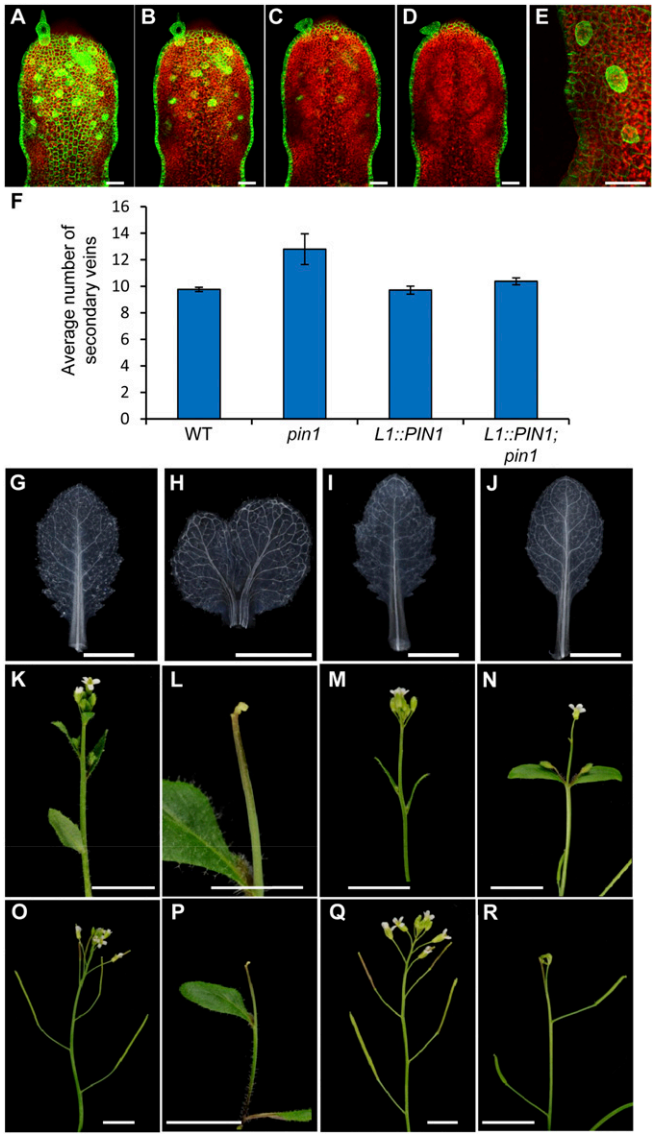

Fig. S2. Epidermal PIN1 activity is sufficient to rescue *pin1* defects. (*A–D*) Serial confocal optical sections of fifth rosette leaf 250 μm in length of *AtML1::PIN1:GFP*. (*E*) Confocal micrograph of *AtML1::PIN1:GFP* at margin of fifth rosette leaf 250 μm in length. (*F*) Quantification of secondary vein number in fifth rosette leaves of wild type, *pin1-7*, *AtML1::PIN1:GFP* (*L1::PIN1*), and *pin1-7; AtML1::PIN1:GFP* (*L1::PIN1;pin1*). (*G–J*) Leaf clearings of fifth rosette leaf of wild type (*G*), *pin1-7* (*H*), *AtML1::PIN1:GFP* (*I*), and *pin1-7;AtML1::PIN1:GFP* (*J*). (*K–N*) Flowers of wild type (*K*), *pin1-7* (*L*), *AtML1::PIN1:GFP* (*M*) and *AtML1::PIN1:GFP;pin1-7* (*N*). (*O–R*) Siliques of wild type (*O*), *pin1-7* (*P*), *AtML1::PIN1:GFP* (*Q*), and *AtML1::PIN1:GFP;pin1-7* (*R*). (Scale bars: *A–D*, 25 μm; *E*, 50 μm; *G–R*, 1 cm.) Error bars represent SE of mean. $n = 15$.

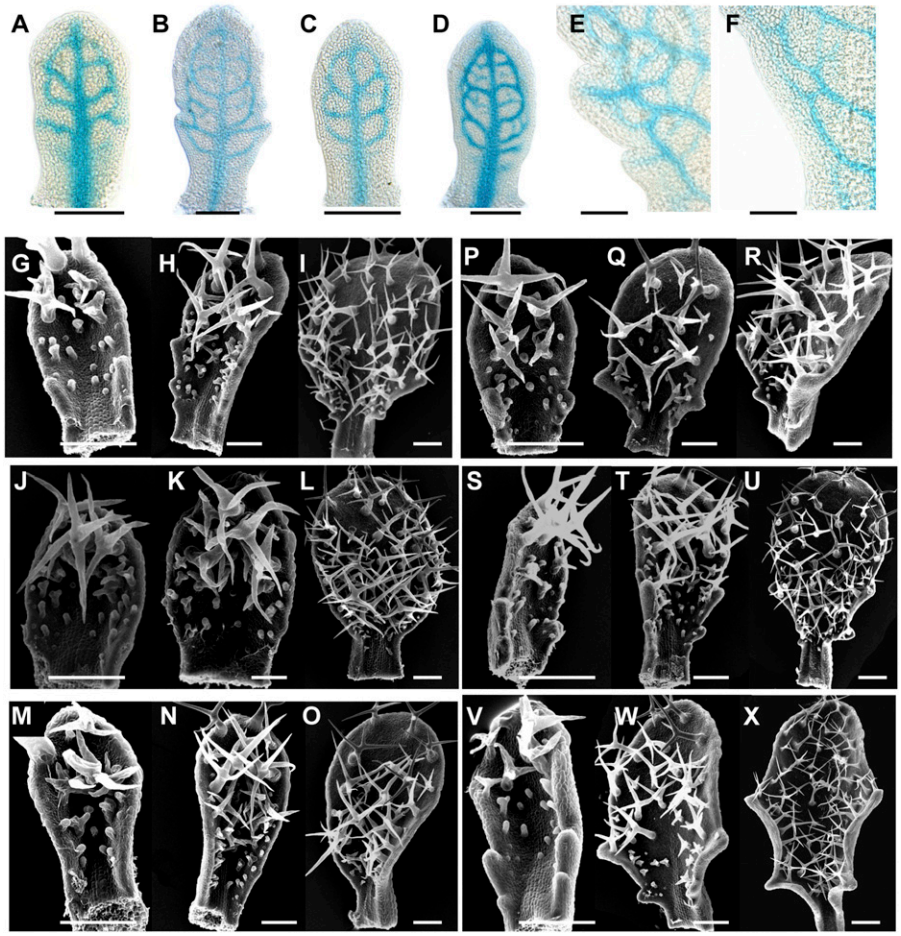

Fig. S3. The processes of serration and vasculature development can be uncoupled in *cuc2* mutants and aberrant CUC2 and PIN1 expression alters margin morphologies. (*A–F*) *ATHB-8::GUS* staining in wild type (*A* and *B*) and *cuc2-3* (*C* and *D*) in eighth rosette leaf 140 μm in length (*A* and *C*) and sixth rosette leaf 220 μm in length (*B* and *D*). Close-up is shown of *ATHB-8::GUS* expression in margin of fifth rosette leaf 350 μm in length in wild type (*E*) and *cuc2-3* (*F*). (*G–O*) Scanning electron micrographs of wild type (*G–I*), *pin1-1* (*J–L*), *cuc2-3* (*M–O*), *mir164a-4* (*P–R*), *axr1-3* (*S–U*), and *bdl/BDL* (*V–X*) for fifth rosette leaf 250 μm in length (*G*, *J*, *M*, *P*, *S*, and *V*), fourth rosette leaf 500 μm in length (*H*, *K*, *N*, *Q*, *T*, and *W*), and third rosette leaf 1,500 μm in length (*I*, *L*, *O*, *R*, *U*, and *X*). (Scale bars: *A–F*, 50 μm; *H* and *I*, *K* and *L*, *N* and *O*, *Q* and *R*, *T* and *U*, and *W* and *X*, 250 μm; and *G*, *J*, *M*, *P*, *S*, and *V*, 125 μm.)

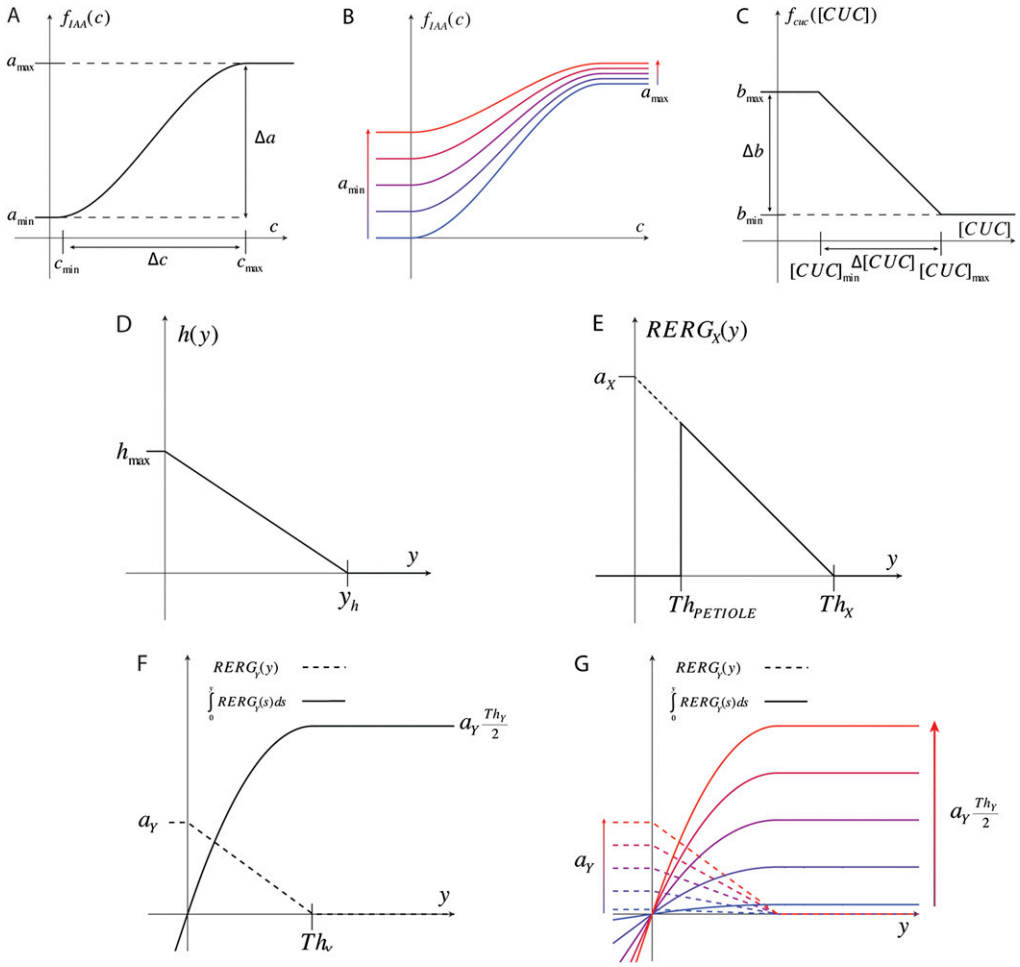

Fig. S4. Plots of functions controlling growth in the model. (*A*) A sigmoidally increasing function $f_{IAA}(c)$ (Eq. S7). (*B*) A family of curves $f_{IAA}(c)$ generated by simultaneously increasing a_{min} and a_{max} (blue to red). (*C*) A decreasing function $f_{CUC}([CUC])$ (Eq. S8). (*D*) A plot of function $h(y)$ (Eq. S9). (*E*) Relative elementary rate of growth $RERG_X$ as a function of y (Eq. S10). The dashed line connects the linearly decreasing segment to its y-intercept a_X . (*F*) Dashed line, the relative elementary rate of growth $RERG_Y$ as a function of y (Eq. S11); solid line, integral of $RERG_Y$ with respect to y (Eq. S15). (*G*) The dependency of curves shown in *F* on the parameter a_y. Corresponding curves are shown in the same color.

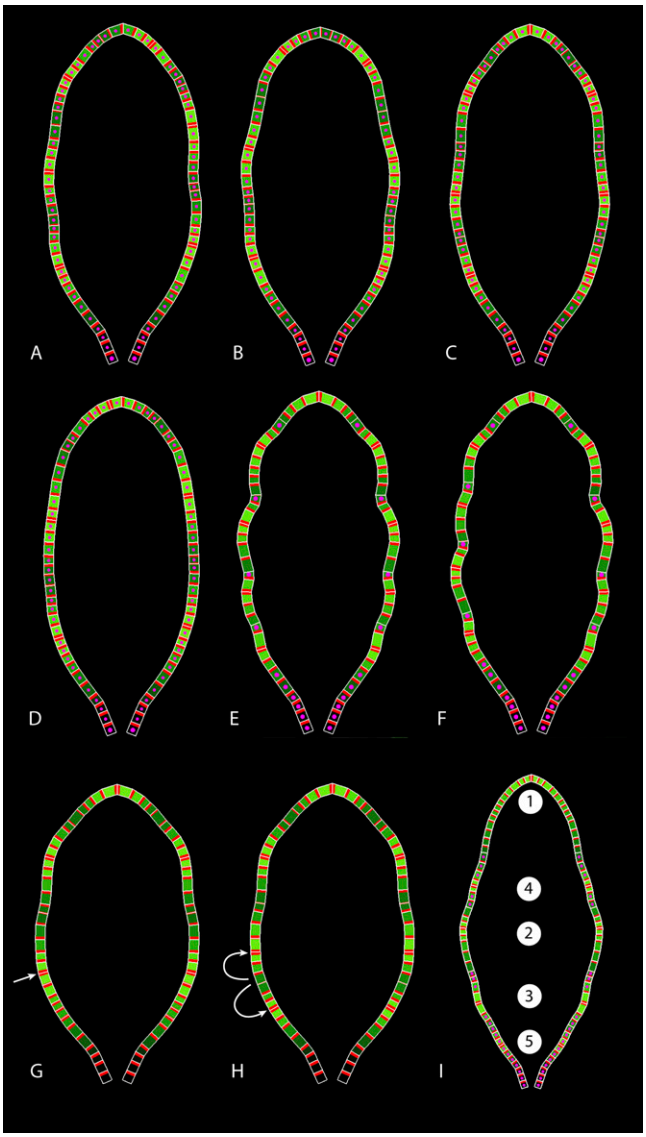

Fig. S5. Analysis of the leaf serration model in the presence of perturbations. (*A*–*C*) Representative *AtML1::CUC2* leaves simulated with the auxin production varying stochastically with uniform distribution in the range of ±2.5% of the maximum production rate σH (Eq. **S1**) in each simulation step. (*D*–*F*) Representative *AtML1::CUC2* (*D*) and wild-type (*E* and *F*) leaves generated with the auxin production varying in the range of ±7.5% of the production rate σH. (*G* and *H*) Snapshots from a simulation of a hypothetical leaf development, in which PIN1 proteins can reorient in the absence of CUC2. The convergence point marked by an arrow (*G*) splits into two convergence points (*H*). The resulting convergence points move away from each other until a stable spacing is achieved (curved arrows). (*I*) The order of serration emergence in a hypothetical leaf growing uniformly along the proximal–distal axis.

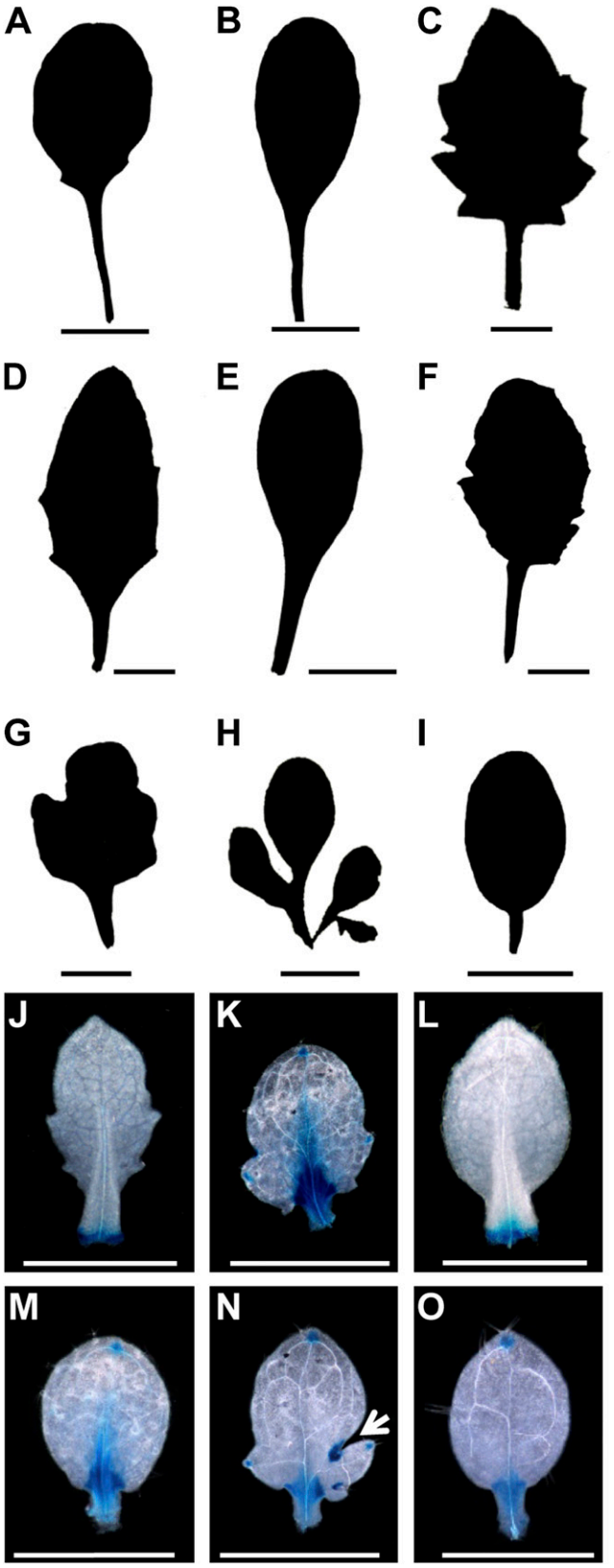

Fig. S6. The CUC2/auxin module influences *jaw-D* and *as1* leaf margin development. (*A–I*) Silhouette of fifth rosette leaf of wild type (*A*), *cuc2-3* (*B*), *jaw-D* (*C*), *jaw-D;cuc2-3* (*D*), *pin1-1* (*E*), *jaw-D;pin1-1* (*F*), *as1-1* (*G*), *axr1-3;as1-1* (*H*), and *axr1-3;as1-1;cuc2-3* (*I*). (*J–O*) *BP::GUS* expression in the fourth rosette leaf of wild type (*J*), *as1-1* (*K*), *cuc2-3* (*L*), *as1-1;cuc2-3* (*M*), *axr1-3;as1-1* (*N*, arrow indicates *BP* misexpression in the sinus region), and *axr1-3;as1-1;cuc2-3* (*O*). (Scale bars: *A–I*, 1 cm; *J–O*, 1.5 mm.)

Table S1. Quantification of dissection index and serration number in auxin signaling mutants in response to loss of *CUC2* function

Genotype	((Perimeter squared)/(4π × area)) ± SE	Average serration no. ± SE
Col	4.46 ± 0.03	4.78 ± 0.29
axr1-3	4.71 ± 0.03	4.24 ± 0.30
axr1-12	6.21 ± 0.16	6.13 ± 0.30
bdl/BDL	5.32 ± 0.06	6.40 ± 0.33
mir164a-4	6.93 ± 0.15	5.93 ± 0.15
cuc2-3	4.19 ± 0.04	0.07 ± 0.07
axr1-3;cuc2-3	3.81 ± 0.03	0.13 ± 0.02
bdl/BDL;cuc2-3	3.70 ± 0.13	0.20 ± 0.02

For leaf dissection index, ANOVA *P* value <0.001 for all genotypes differing from wild type. For serration number, ANOVA *P* value <0.001 for all genotypes differing from wild type other than *axr1-3*, which has deeper serrations, but not significantly different serration number compared with wild type. This discrepancy is not observed in the stronger allele, *axr1-12*, which has both an increased number and increased depth of serrations compared with wild type. Quantifications were performed in the fifth rosette leaf, *n* = 15.

Table S2. Parameter values related to the simulation of molecular-level processes

Parameter			Simulation						
Name	Symbol	Equation	Fig. 5 *C–H*, wild type	Fig. 5*I*, *pin1*	Fig. 5*J*, auxin application	Fig. 5*K*, CUC2	Fig. 5*L*, CUC2 overexpression	Fig. 5*M*, L1::CUC	Movie S7
Polar transport coefficient	T	S2	0.4						
Diffusion coefficient	D	S2	2.5	1.5					
Auxin production rate	σ	S1	0.4						
Target auxin concentration	H	S1	10						
Auxin turnover rate	μ	S1	0.005						
Exogenous auxin flux	Φ_{ext}	S1	0		0.8				
PIN1 concentration	$[PIN_i]$	S3	1	0					
Exponentiation base for calculating PIN1 polarization	b	S3	6						
Threshold CUC2 concentration for PIN1 polarization	Th_{CUC}	S4	1						0
CUC2 production rate	ρ_{CUC}	S5	63						
Sensitivity of CUC2 down-regulation to auxin	κ_{CUC}	S5	1.7						
CUC2 turnover rate	ν	S5	3.6						
Coefficient of auxin-dependent CUC2 degradation rate	ν_{IAA}	S5	0.0018						
Maximum CUC2 concentration	CUC_{MAX}	S5	5			0*	15	5†	0
Time step for molecular-level simulations			0.05						

All simulations use the same parameter values as specified for the wild-type leaf (fourth column) except when shown otherwise.
*PIN1 can reorient for the first 180 frames, allowing the convergence point at the leaf apex to form.
†The concentration of CUC2 is constant in each cell over time.

Table S3. Parameter values related to growth regulation

Name	Symbol	Equation	Value
Minimum value of f_{IAA}	a_{min}	S7	0.1
Maximum value of f_{IAA}	a_{max}	S7	1.0
Range of margin displacement rate sensitivity to auxin concentration	(c_{min}, c_{max})	S7	[0, 15]
Minimum value of f_{CUC}	b_{min}	S8	0
Maximum value of f_{CUC}	b_{max}	S8	1
Range of margin displacement rate sensitivity to CUC concentration	($[CUC]_{min}$, $[CUC]_{max}$)	S8	[0, 55]
Maximum margin displacement rate	h_{max}	S9	0.0396
Longitudinal extent of margin displacement	y_h	S9	600
Longitudinal extent of lateral growth inhibition	$Th_{PETIOLE}$	S10	100
Maximum rate of lateral growth	a_x	S10	0.00825
Longitudinal extent of lateral growth	Th_x	S10	300
Maximum rate of longitudinal growth	a_Y	S11	0.01650
Longitudinal extent of longitudinal growth	Th_y	S11	300
Threshold length for cell division	Th_{length}	—	50
Time step for growth simulation			2.5

Table S4. Alleles and transgenic lines

Allele	Background	Reference
axr1-3	Col	CS3374, ABRC
axr1-12	Col	N3076, NASC
as1-1	Col	CS3075, ABRC
bdl/BDL	Col	(1)
cuc2-3	Col	(2)
mir164a-4	Col	(3)
pin1-1	Col	(4) Isolated in Enkheim and backcrossed to Col five times
pin1-7	Col	(5)
ATHB-8::GUS	Col	(6)
CUC2::CUC2:VENUS	Col	(7) Transformed in Col
CUC2::GUS	Col	(2)
CUC2gm-4	Col	(3)
DR5::GFP	Col	(8)
MIR164A::GUS	Col	(3)
PIN1::PIN1:GFP	Col	(8)
jaw-D	Col	(9)

1. Hamann T, Mayer U, Jürgens G (1999) The auxin-insensitive *bodenlos* mutation affects primary root formation and apical-basal patterning in the Arabidopsis embryo. *Development* 126:1387–1395.
2. Hibara K, et al. (2006) Arabidopsis CUP-SHAPED COTYLEDON3 regulates postembryonic shoot meristem and organ boundary formation. *Plant Cell* 18:2946–2957.
3. Nikovics K, et al. (2006) The balance between the MIR164A and CUC2 genes controls leaf margin serration in Arabidopsis. *Plant Cell* 18:2929–2945.
4. Blilou I, et al. (2005) The PIN auxin efflux facilitator network controls growth and patterning in Arabidopsis roots. *Nature* 433:39–44.
5. Smith R-S, et al. (2006) A plausible model of phyllotaxis. *Proc Natl Acad Sci USA* 103:1301–1306.
6. Baima S, et al. (1995) The expression of the *Athb-8* homeobox gene is restricted to provascular cells in *Arabidopsis thaliana*. *Development* 121:4171–4182.
7. Heisler M-G, et al. (2005) Patterns of auxin transport and gene expression during primordium development revealed by live imaging of the Arabidopsis inflorescence meristem. *Curr Biol* 15:1899–1911.
8. Benková E, et al. (2003) Local, efflux-dependent auxin gradients as a common module for plant organ formation. *Cell* 115:591–602.
9. Palatnik J-F, et al. (2003) Control of leaf morphogenesis by microRNAs. *Nature* 425:257–263.

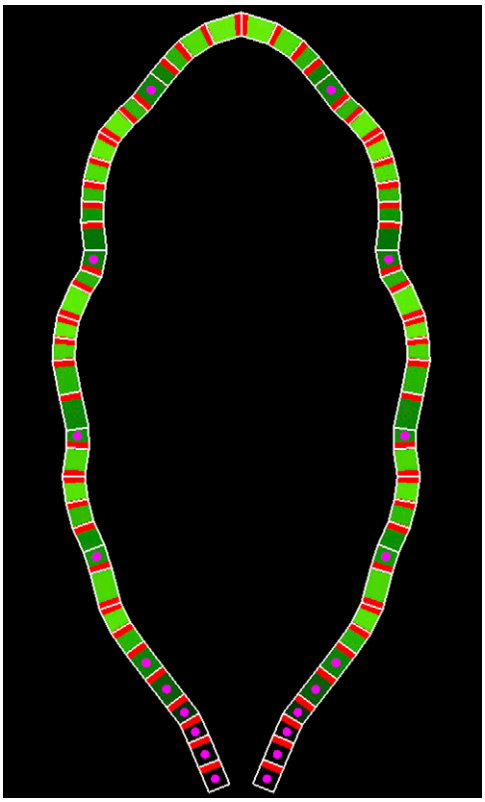

Movie S1. Simulation of wild-type leaf development (corresponds to Fig. 5 *C–H*).

Movie S1

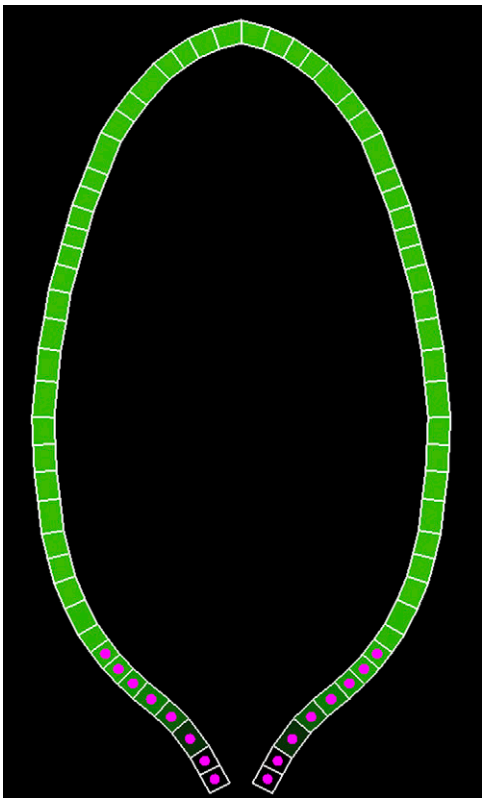

Movie S2. Simulation of *pin1* leaf development (corresponds to Fig. 5*I*).

Movie S2

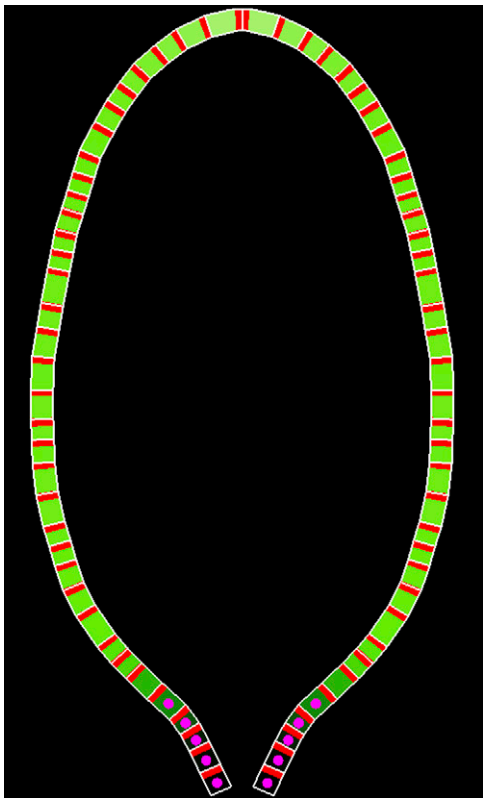

Movie S3. Simulation of leaf development with exogenously applied auxin (corresponds to Fig. 5*J*).

Movie S3

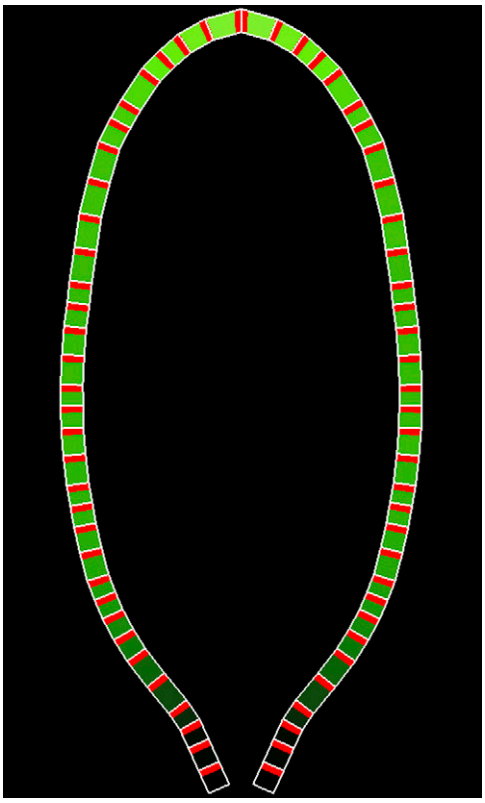

Movie S4. Simulation of *cuc2* leaf development (corresponds to Fig. 5*K*).

Movie S4

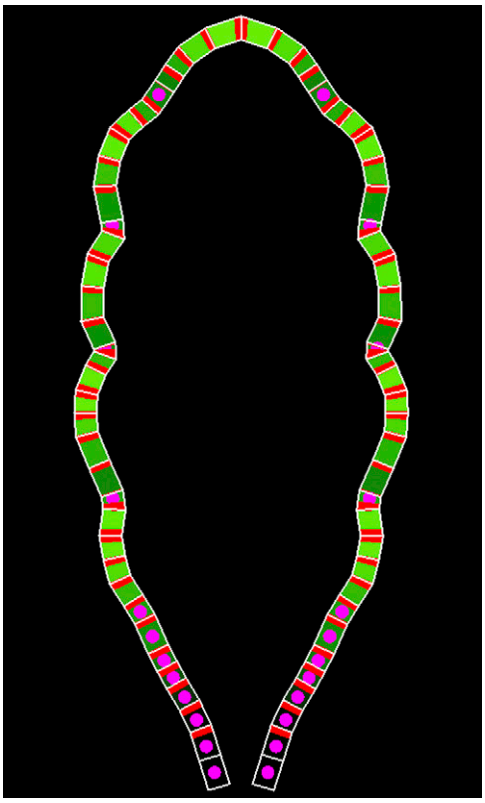

Movie S5. Simulation of leaf development with increased CUC2 expression (as seen in *axr1*, *bdl*/*BDL*, and *mir164a* mutants) (corresponds to Fig. 5*L*).

Movie S5

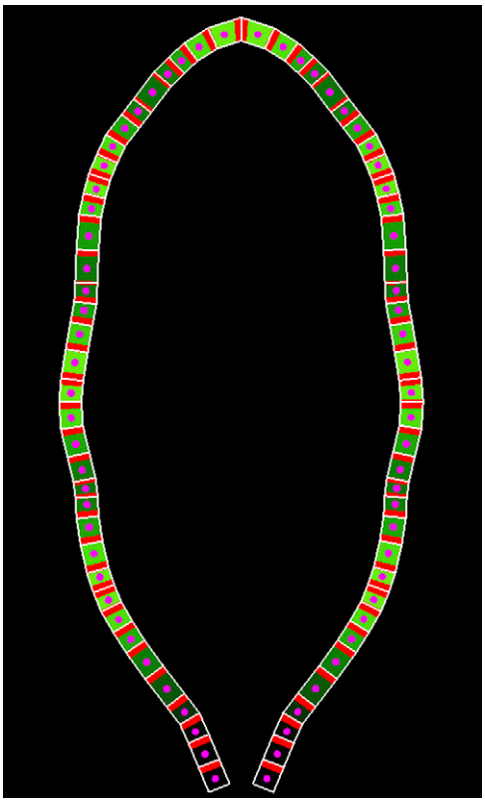

Movie S6. Simulation of L1::CUC2 leaf development (corresponds to Fig. 5*M*).

Movie S6

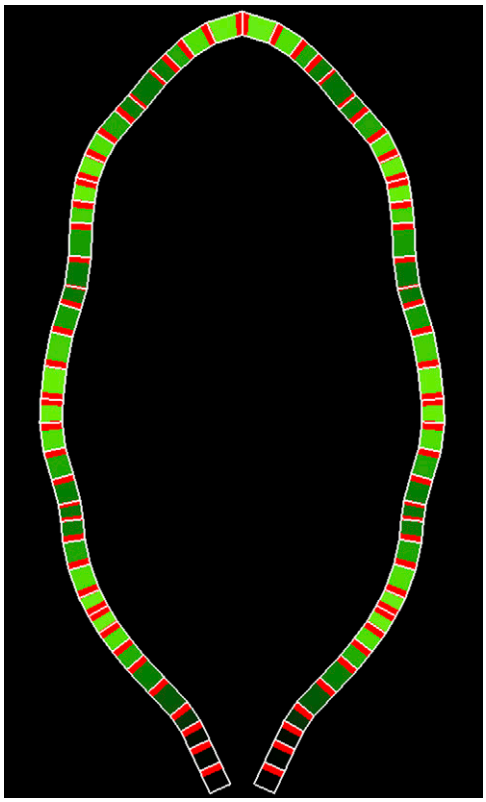

Movie S7. Simulation of leaf form development, in which PIN1 can reorient in the absence of CUC2 (corresponds to Fig. S5 *G* and *H*). The number of convergence points is reduced with respect to the wild type. The sustained ability of PIN1 proteins to reorient at convergence points also results in different dynamics of auxin and PIN1 distribution. Specifically, auxin maxima travel along the margin, and following the establishment of the first pair of convergence points, subsequent convergence points form due to the splitting of the most proximal points into two. Similar dynamics are observed in the simulations of L1::CUC2 leaves (Movie S6).

Movie S7

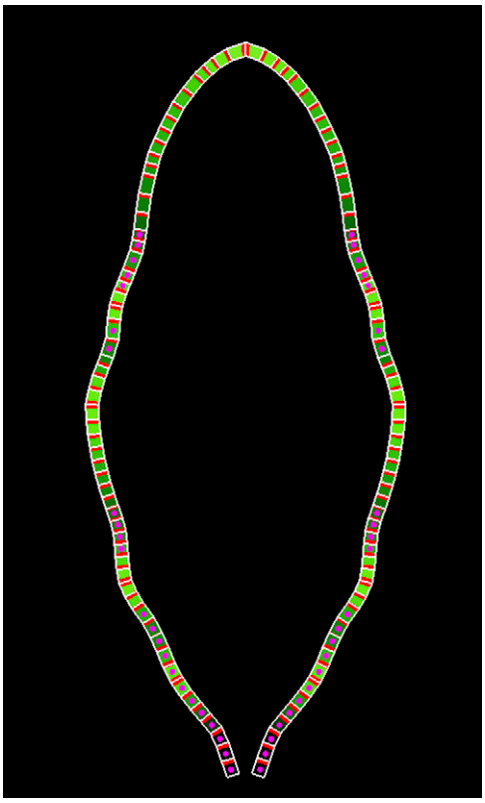

Movie S8. Intercallary emergence of serrations in a hypothetical leaf growing uniformly along the proximal–distal axis (corresponds to Fig. S5*I*).

Movie S8

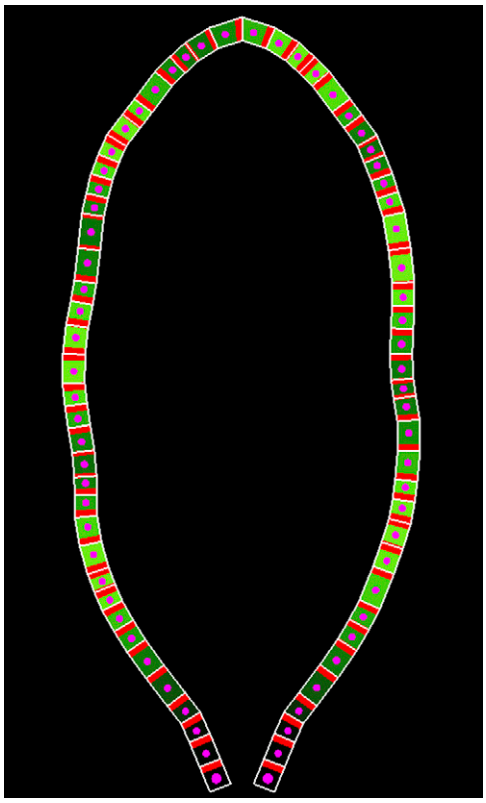

Movie S9. Development of an *AtML1::CUC2* leaf simulated with the auxin production varying stochastically with uniform distribution in the range of ±2.5% of the maximum production rate σH (Eq. **S1**) in each simulation step (corresponds to Fig. S5*A*).

Movie S9

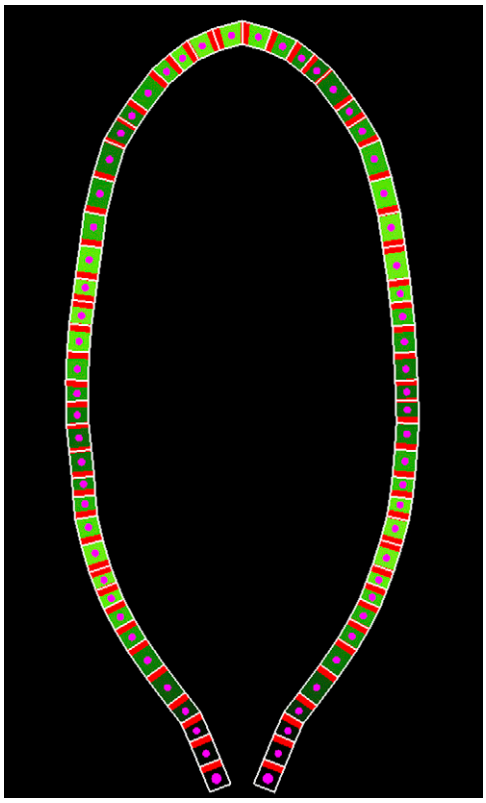

Movie S10. Development of a *AtML1::CUC2* leaf simulated with the auxin production varying stochastically with uniform distribution in the range of ±7.5% of the maximum production rate σH (Eq. **S1**) in each simulation step (corresponds to Fig. S5*D*).

Movie S10

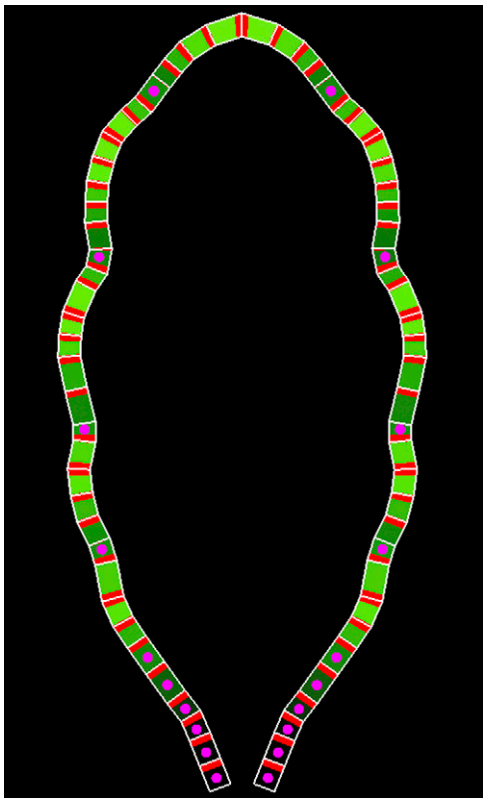

Movie S11. Development of a wild-type leaf simulated with the auxin production varying stochastically with uniform distribution in the range of ±7.5% of the maximum production rate σH (Eq. **S1**) in each simulation step (corresponds to Fig. *S5E*).

Movie S11